A&A 563, A143 (2014)
DOI: 10.1051/0004-6361/201323204

Astronomy & Astrophysics

Transiting planets from WASP-South, Euler, and TRAPPIST

WASP-68 b, WASP-73 b, and WASP-88 b, three hot Jupiters transiting evolved solar-type stars⋆,⋆⋆

L. Delrez[1], V. Van Grootel[1,⋆⋆⋆], D. R. Anderson[2], A. Collier-Cameron[3], A. P. Doyle[2], A. Fumel[1], M. Gillon[1], C. Hellier[2], E. Jehin[1], M. Lendl[4], M. Neveu-VanMalle[4,6], P. F. L. Maxted[2], F. Pepe[4], D. Pollacco[5], D. Queloz[6,4], D. Ségransan[4], B. Smalley[2], A. M. S. Smith[7,2], J. Southworth[2], A. H. M. J. Triaud[8,4,⋆⋆⋆⋆], S. Udry[4], and R. G. West[5]

[1] Institut d'Astrophysique et Géophysique, Université de Liège, allée du 6 Août 17, 4000 Liège, Belgium
e-mail: ldelrez@ulg.ac.be
[2] Astrophysics Group, Keele University, Staffordshire, ST5 5BG, UK
[3] SUPA, School of Physics and Astronomy, University of St. Andrews, North Haugh, Fife, KY16 9SS, UK
[4] Observatoire de Genève, Université de Genève, 51 Chemin des Maillettes, 1290 Sauverny, Switzerland
[5] Department of Physics, University of Warwick, Coventry CV4 7AL, UK
[6] Cavendish Laboratory, Department of Physics, University of Cambridge, JJ Thomson Avenue, Cambridge, CB3 0HE, UK
[7] N. Copernicus Astronomical Centre, Polish Academy of Sciences, Bartycka 18, 00-716 Warsaw, Poland
[8] Department of Physics and Kavli Institute for Astrophysics & Space Research, Massachusetts Institute of Technology, Cambridge MA 02139, USA

Received 6 December 2013 / Accepted 18 January 2014

ABSTRACT

Using the WASP transit survey, we report the discovery of three new hot Jupiters, WASP-68 b, WASP-73 b and WASP-88 b. The planet WASP-68 b has a mass of 0.95 ± 0.03 $M_{\rm Jup}$, a radius of $1.24^{+0.10}_{-0.06}$ $R_{\rm Jup}$, and orbits a V = 10.7 G0-type star (1.24 ± 0.03 $M_\odot$, $1.69^{+0.11}_{-0.06}$ $R_\odot$, $T_{\rm eff}$ = 5911 ± 60 K) with a period of 5.084298 ± 0.000015 days. Its size is typical of hot Jupiters with similar masses. The planet WASP-73 b is significantly more massive ($1.88^{+0.07}_{-0.06}$ $M_{\rm Jup}$) and slightly larger ($1.16^{+0.12}_{-0.08}$ $R_{\rm Jup}$) than Jupiter. It orbits a V = 10.5 F9-type star ($1.34^{+0.05}_{-0.04}$ $M_\odot$, $2.07^{+0.19}_{-0.08}$ $R_\odot$, $T_{\rm eff}$ = 6036 ± 120 K) every 4.08722 ± 0.00022 days. Despite its high irradiation (~2.3 × 10^9 erg s^{-1} cm^{-2}), WASP-73 b has a high mean density ($1.20^{+0.26}_{-0.30}$ $\rho_{\rm Jup}$) that suggests an enrichment of the planet in heavy elements. The planet WASP-88 b is a 0.56 ± 0.08 $M_{\rm Jup}$ hot Jupiter orbiting a V = 11.4 F6-type star (1.45 ± 0.05 $M_\odot$, $2.08^{+0.12}_{-0.06}$ $R_\odot$, $T_{\rm eff}$ = 6431 ± 130 K) with a period of 4.954000 ± 0.000019 days. With a radius of $1.70^{+0.13}_{-0.07}$ $R_{\rm Jup}$, it joins the handful of planets with super-inflated radii. The ranges of ages we determine through stellar evolution modeling are 4.5–7.0 Gyr for WASP-68, 2.8-5.7 Gyr for WASP-73 and 1.8–4.3 Gyr for WASP-88. The star WASP-73 appears to be significantly evolved, close to or already in the subgiant phase. The stars WASP-68 and WASP-88 are less evolved, although in an advanced stage of core H-burning.

Key words. planetary systems – techniques: photometric – techniques: radial velocities – techniques: spectroscopic

1. Introduction

Since the discovery of the first extrasolar planet around a solar-type star by Mayor & Queloz (1995), more than 1000 planets have been detected outside our solar system[1]. Among this large harvest, the sub-sample of planets that transit the disc of their host star is extremely valuable. Indeed, transiting exoplanets allow parameters such as mass, radius, and density to be accurately determined (e.g. Charbonneau et al. 2000), and their atmospheric properties to be studied during their transits and occultations (e.g. Seager & Deming 2010). At the time of writing, over 400 transiting planets have been discovered[1]; a significant fraction of them are Jovian-type planets orbiting within 0.1 AU of their host star. Most of these so-called "hot Jupiters" were detected by ground-based transit surveys, among which the Wide Angle Search for Planets (WASP) survey (Pollacco et al. 2006) has been the most successful with now more than 100 planets discovered (Hellier et al. 2013). Ongoing WASP discoveries are important for the field of exoplanetology, as these systems tend to be particularly prone to thorough characterizations, owing to their bright host stars ($9 < V < 13$), short orbits, and favorable planet-to-star area ratios. Therefore, they will be prime targets for thorough characterizations with future facilities, such as CHaracterising ExOPlanets Satellite (CHEOPS, Broeg et al. 2013) and *James Webb* Space Telescope (JWST, Gardner et al. 2006).

In this paper, we report the discovery of three additional transiting planets by the WASP survey. The planet WASP-68 b is a 0.95 $M_{\rm Jup}$ hot Jupiter in a 5 days orbit around a G0-type star; WASP-73 b is a dense 1.88 $M_{\rm Jup}$ planet that

⋆ Tables 1–3 are available in electronic form at http://www.aanda.org

⋆⋆ The photometric time-series used in this work are only available at the CDS via anonymous ftp to cdsarc.u-strasbg.fr (130.79.128.5) or via http://cdsarc.u-strasbg.fr/viz-bin/qcat?J/A+A/563/A143

⋆⋆⋆ Chargée de recherches, Fonds de la Recherche Scientifique, FNRS, rue d'Egmont 5, 1000 Bruxelles, Belgium.

⋆⋆⋆⋆ Fellow of the Swiss National Science Foundation.

[1] http://exoplanet.eu/

orbits an F9-type star every 4.1 days, while WASP-88 b is a super-bloated 0.56 $M_{\rm Jup}$ planet in a 4.9 days orbit around an F6-type star. All three host stars appear to be significantly evolved. Consequently, they have relatively large radii ($R_\star$ = 1.7–2.1 $R_\odot$), translating into long (5–6 h) and low-amplitude transits for the three planets: ~0.6% for WASP-68 b, ~0.3% for WASP-73 b (the shallowest transits yet for a WASP planet), and ~0.7% for WASP-88 b. Their detection demonstrates, therefore, the excellent photometric potential of the WASP survey.

Section 2 presents the WASP discovery photometry, as well as the follow-up photometric and spectroscopic observations that we used to confirm and characterize the three systems. In Sect. 3, we describe the spectroscopic determination of the stellar atmospheric properties and the derivation of the systems' parameters through combined analyses of our photometric and spectroscopic data. Finally, we discuss and summarize our results in Sect. 4.

2. Observations

2.1. WASP transit detection photometry

The WASP transit survey is operated from two sites with one for each hemisphere: the Observatorio del Roque de los Muchachos in the Canary Islands in the North and the Sutherland Station of the South African Astronomical Observatory (SAAO) in the South. Each facility consists of eight Canon 200 mm f/1.8 focal lenses coupled to e2v 2048 × 2048 pixels CCDs, which yields a field of view of 450 deg^2 for each site with a corresponding pixel scale of 13.7″/pixel. Further details of the instruments, survey, and data reduction procedures can be found in Pollacco et al. (2006), while details of the candidate selection process can be found in Collier Cameron et al. (2006, 2007). The three targets presented here, WASP-68 (1SWASPJ202022.98-191852.9 = 2MASS20202298-1918528, V = 10.7, K = 8.9), WASP-73 (1SWASPJ211947.91-580856.0 = 2MASS21194790-5808559, V = 10.5, K = 9.0), and WASP-88 (1SWASPJ203802.70-482743.2 = 2MASS20380268-4827434, V = 11.4, K = 10.3), were observed exclusively from the southern WASP site. In total, 20 804 data points were obtained for WASP-68 between May 2006 and October 2011, 50 588 measurements were gathered for WASP-73 between June 2008 and November 2011, while 39 906 data points were obtained for WASP-88 between June 2008 and October 2011. For each target, the WASP data were processed and searched for transit signals, as described in Collier Cameron et al. (2006), leading to the detection of periodic dimmings in the light curves of WASP-68, –73 and –88 with periods of 5.084 d, 4.087 d and 4.954 d, respectively. For the three objects, Fig. 1 presents the WASP photometry folded on the deduced transit ephemeris.

The method described in Maxted et al. (2011) was used to search for rotational modulation in the photometry of each object. The analysis was performed over the frequency interval 0–1.5 cycles/day at 8192 evenly spaced frequencies. No periodic signal was found above the mmag amplitude.

2.2. Spectroscopy and radial velocities

Spectroscopic measurements of each star were obtained using the CORALIE spectrograph mounted on the 1.2 m Euler-Swiss telescope at the La Silla site (Chile). A total of 43 spectra were gathered for WASP-68 between May 2011 and August 2013; 20 spectra were obtained for WASP-73 from October 2011 to September 2013, while 23 spectra were gathered for WASP-88 between September 2011 and October 2013. For all spectroscopic observations, radial velocities (RVs) were computed using the weighted cross-correlation technique described in Pepe et al. (2002). These RVs are presented in Tables 1–3. For each star, RV variations were detected with periods similar to those found in the WASP photometry and with semi-amplitudes consistent with planetary-mass companions (see Figs. 2, 4, and 6, upper panels).

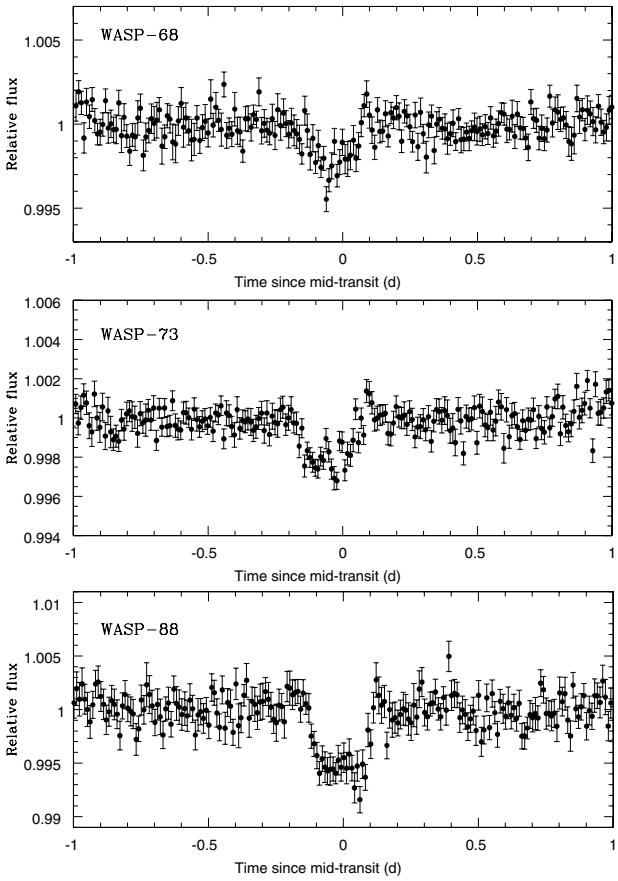

Fig. 1. WASP photometry for WASP-68 (*top*), WASP-73 (*middle*), and WASP-88 (*bottom*) folded on the best-fitting transit ephemeris from the transit search algorithm presented in Collier Cameron et al. (2006), and binned per 0.01 d intervals.

To discard any false-positive scenarios that could create RV variations that mimic planetary signatures, we checked the CORALIE cross-correlation functions (CCF) bisector spans, according to the technique described by Queloz et al. (2001). Indeed, false positives, such as blended eclipsing binaries or starspots, would also induce spectral-line distortions, resulting in correlated variations of RVs and bisector spans. This effect was, for example, observed for the HD 41004 system (Santos et al. 2002), which consists of a K-dwarf blended with an M-dwarf companion (separation of ~0.5″) that is orbited itself by a short-period brown dwarf. For this extreme system, the RVs showed a clear signal at the period of the brown dwarf orbit (1.3 d) and with an amplitude ~50 m s^{-1} that could have been interpreted as the signal of a sub-Saturn mass planet orbiting the K-dwarf. However, the 0.67 ± 0.03 slope of the RV-bisector relation clearly revealed that the observed signal did not originate from the K-dwarf and shed light on the blended nature of the system.

For our three systems, the bisector spans revealed to be stable; their standard deviation are close to their average error

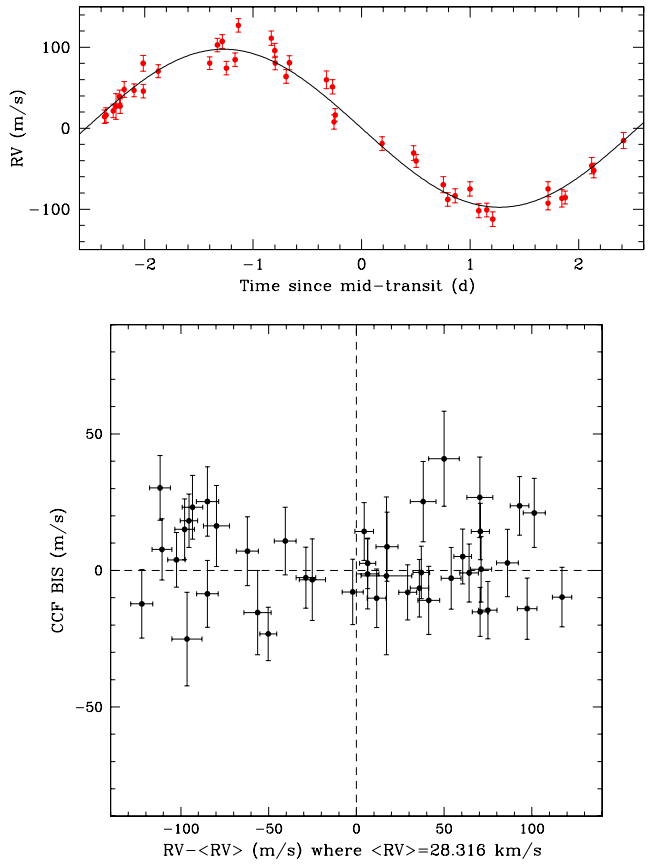

Fig. 2. *Top*: CORALIE RVs for WASP-68 phase-folded on the best-fit orbital period with the best-fit Keplerian model over-imposed in red. *Bottom*: correlation diagram CCF bisector span vs. RV.

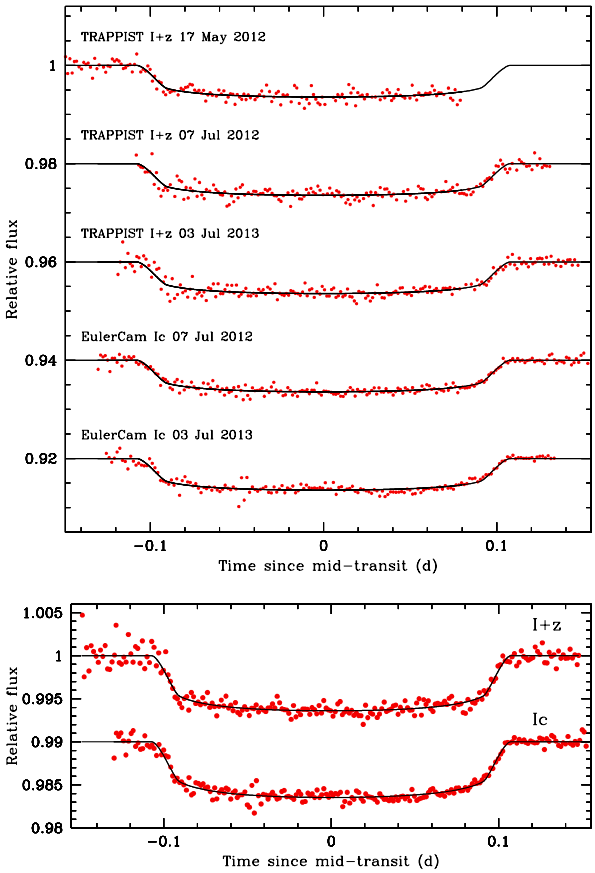

Fig. 3. *Top*: individual follow-up transit light curves for WASP-68 b. *Bottom*: combined follow-up photometry for WASP-68 b. The observations are shown as red points (bin width =2min) and are period-folded on the best-fit transit ephemeris. Each light curve has been divided by the respective photometric baseline model (see Sect. 3.2). For each filter, the superimposed, solid black line is our best-fit transit model. The light curves are shifted along the *y*-axis for clarity.

(15 vs. 12 m s^{-1} for WASP-68, 27 vs. 18 m s^{-1} for WASP-73 and 48 vs. 45 m s^{-1} for WASP-88). No correlation between the RVs and the bisector spans was found (see Figs. 2, 4, and 6, lower panels); the slopes deduced from linear regressions were −0.01 ± 0.03 (WASP-68), 0.04 ± 0.05 (WASP-73), and 0.10 ± 0.21 (WASP-88). These values and errors support our conclusion that the periodic dimming and RV variation of each system are caused by a transiting planet. This conclusion is also strengthened by the consistency of the solutions derived from the global analysis of our spectroscopic and photometric data (see Sect. 3.2).

2.3. Follow-up photometry

To refine the systems' parameters, high-quality transit observations were obtained using the 0.6 m TRAPPIST robotic telescope (TRAnsiting Planets and PlanetesImals Small Telescope) and the EulerCam CCD camera that is mounted on the 1.2 m Euler-Swiss telescope, which are both located at ESO La Silla Observatory. These follow-up light curves are summarized in Table 4 and presented in Figs. 3, 5, and 7.

2.3.1. TRAPPIST observations

TRAPPIST is a 60 cm robotic telescope dedicated to the detection and characterization of transiting exoplanets and to the photometric monitoring of bright comets and other small bodies. It is equipped with a thermoelectrically-cooled 2K × 2K CCD, which has a pixel scale of 0.65″ that translates into a 22′ × 22′ field of view. For details of TRAPPIST, see Gillon et al. (2011b) and Jehin et al. (2011). The TRAPPIST photometry was obtained using a readout mode of 2 × 2 MHz with 1 × 1 binning, which results in a readout + overhead time of 6.1 s and a readout noise of 13.5 e$^-$. A slight defocus was applied to the telescope to improve the duty cycle, spread the light over more pixels, and, thereby, improve the sampling of the PSF. Three transits of WASP-68 b and two transits of WASP-88 b were observed through a special "$I + z$" filter that has a transmittance >90% from 750 nm to beyond 1100 nm[2]. For WASP-73b, two transits were observed in a Sloan z' filter ($\lambda_{\rm eff}$ = 915.9 ± 0.5 nm). During the runs, the positions of the stars on the chip were maintained to within a few pixels thanks to a "software guiding" system that regularly derives an astrometric solution for the most recently acquired image and sends pointing corrections to the mount if needed. After a standard pre-reduction (bias, dark, and flatfield correction), the stellar fluxes were extracted from the images using the IRAF/DAOPHOT[3] aperture photometry software (Stetson 1987). For each light curve, we tested several sets

[2] http://www.astrodon.com/products/filters/near-infrared/

[3] IRAF is distributed by the National Optical Astronomy Observatory, which is operated by the Association of Universities for Research in Astronomy, Inc., under cooperative agreement with the National Science Foundation.

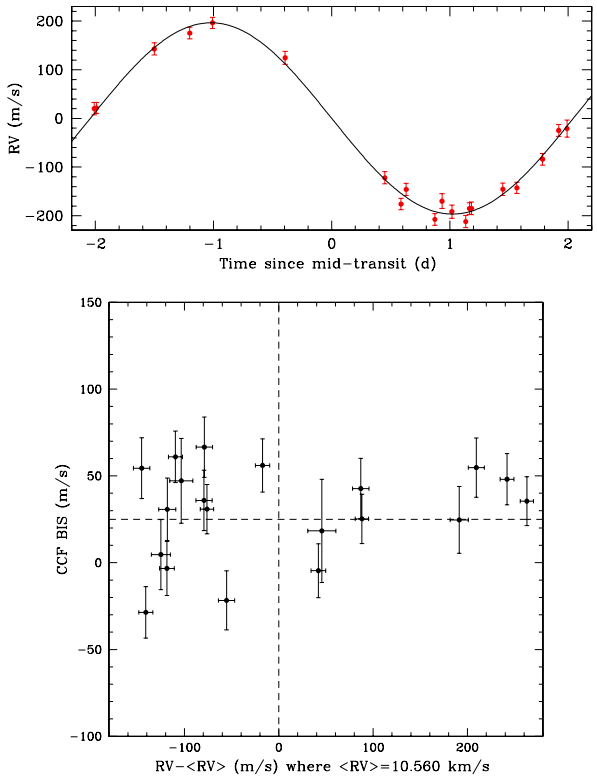

Fig. 4. *Top*: CORALIE RVs for WASP-73 phase-folded on the best-fit orbital period with the best-fit Keplerian model over-imposed in red. *Bottom*: correlation diagram CCF bisector span vs. RV.

of reduction parameters and kept the one giving the most precise photometry for the stars of similar brightness as the target. After a careful selection of reference stars, the transit light curves were finally obtained using differential photometry.

2.3.2. EulerCam observations

EulerCam is an E2V 4K × 4K back-illuminated, deep-depletion CCD detector installed at the Cassegrain focus of the 1.2 m Euler-Swiss telescope. The field of view of EulerCam is 15.7′ × 15.7′, producing a pixel scale of 0.23″. To keep the stars on the same locations on the detector during the observations, EulerCam employs an "Absolute Tracking" system that is very similar to the one of TRAPPIST, which matches the point sources in each image with a catalog, and if needed, adjusts the telescope pointing between exposures to compensate for drifts. Two transits of WASP-73 b and three transits of WASP-88 b were observed with EulerCam through Gunn-r' filter ($\lambda_{\rm eff}$ = 620.4 ± 0.5 nm), while two transits of WASP-68 b were observed in an I_c filter ($\lambda_{\rm eff}$ = 806 ± 0.5 nm). A slight defocus was applied to the telescope to optimize the observation efficiency and to minimize pixel-to-pixel effects. The reduction procedure used to extract the transit light curves was similar to that performed on TRAPPIST data. Further details of the EulerCam instrument and data reduction procedures can be found in Lendl et al. (2012).

3. Analysis

3.1. Spectroscopic analysis: Stellar atmospheric properties

For each star, the individual CORALIE spectra were co-added to produce a single spectrum with a typical S/N of around 100:1.

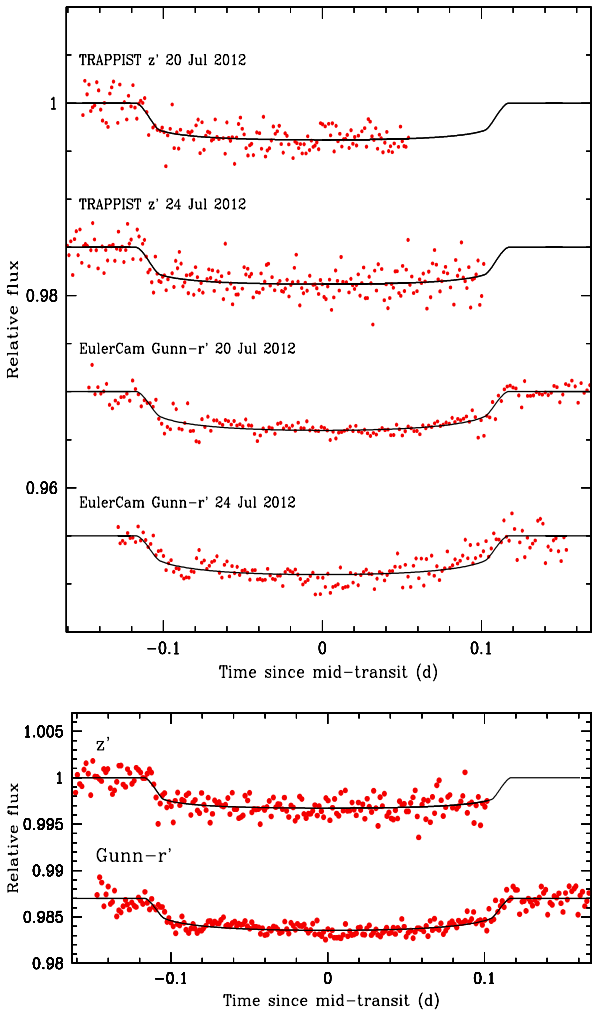

Fig. 5. *Top*: individual follow-up transit light curves for WASP-73 b. *Bottom*: combined follow-up photometry for WASP-73 b. The observations are shown as red points (bin width =2 min) and are period-folded on the best-fit transit ephemeris. Each light curve has been divided by the respective photometric baseline model (see Sect. 3.2). For each filter, the superimposed, solid black line is our best-fit transit model. The light curves are shifted along the y-axis for clarity.

The stellar atmospheric parameters were then derived using the methods given in Doyle et al. (2013). These parameters are listed in Tables 6–8 for WASP-68, WASP-73, and WASP-88, respectively. The excitation balance of the Fe I lines was used to determine the effective temperature $T_{\rm eff}$. The surface gravity log $g_\star$ was determined from the ionisation balance of Fe I and Fe II. The Ca I line at 6439 Å and the Na I D lines were also used as $log\, g_\star$ diagnostics. The elemental abundances were determined from equivalent width measurements of several unblended lines. Iron abundances are relative to the solar values obtained by Asplund et al. (2009). Values for microturbulence ($\xi_{\rm t}$) were determined from Fe I using the method of Magain (1984). The quoted error estimates include that given by the uncertainties in $T_{\rm eff}$ and log $g_\star$, as well as the scatter due to measurement and atomic data uncertainties. The projected stellar rotation velocity v sin $i_\star$ was determined by fitting the profiles of several unblended Fe I lines. An instrumental FWHM of 0.11 ± 0.01 Å was determined for the three stars from the telluric lines around 6300 Å. Macroturbulence ($v_{\rm mac}$) values were obtained from the calibration of Bruntt et al. (2010). Spectral

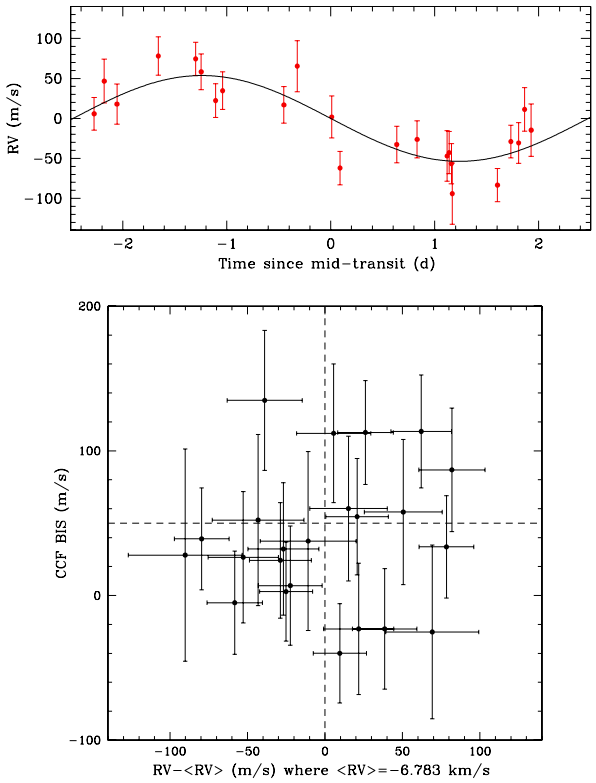

Fig. 6. *Top*: CORALIE RVs for WASP-88 phase-folded on the best-fit orbital period with the best-fit Keplerian model over-imposed in red. *Bottom*: correlation diagram CCF bisector span vs. RV.

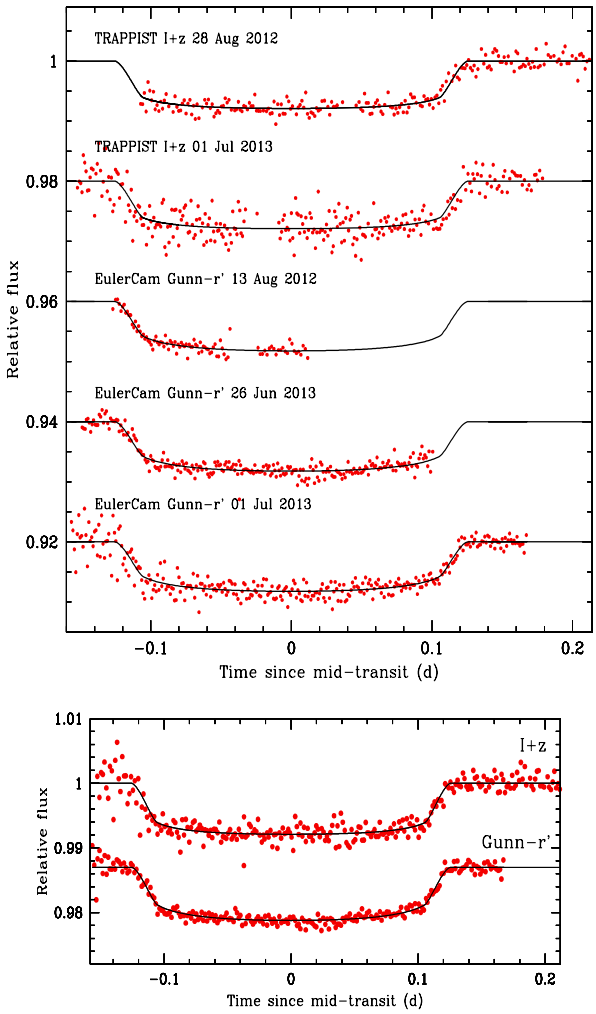

Fig. 7. *Top*: individual follow-up transit light curves for WASP-88 b. *Bottom*: combined follow-up photometry for WASP-88 b. The observations are shown as red points (bin width =2min) and are period-folded on the best-fit transit ephemeris. Each light curve has been divided by the respective photometric baseline model (see Sect. 3.2). For each filter, the superimposed, solid black line is our best-fit transit model. The light curves are shifted along the *y*-axis for clarity.

types were estimated from $T_{\rm eff}$ using the table in Gray (2008). Finally, we also used the Torres et al. (2010) calibration to obtain first stellar mass estimates: 1.24 ± 0.10 $M_\odot$ for WASP-68, 1.40 ± 0.12 $M_\odot$ for WASP-73, and 1.38 ± 0.12 $M_\odot$ for WASP-88.

3.2. Global analysis

To determine the parameters of each system, we performed a combined analysis of the follow-up photometry and the RV data, using for this purpose the adaptive Markov chain Monte-Carlo (MCMC) code described in Gillon et al. (2012) and references therein. The algorithm simultaneously models the data, using for the photometry, the transit model by Mandel & Agol (2002) multiplied by a different baseline model for each light curve, and a classical Keplerian model for the RVs (e.g. Murray & Correia 2010).

The photometric baseline models aim to represent astrophysical, instrumental, or environmental effects, which are able to produce photometric variations and can, therefore, affect the transit light curves. They are made up of different first to fourth-order polynomials with respect to time or other variables, such as airmass, PSF full-width at half maximum, background, or stellar position on the detector. To find the optimal baseline function for each light curve, i.e. the model minimizing the number of parameters and the level of noise in the best-fit residuals, the Bayes factor, as estimated from the Bayesian Information Criterion (Schwarz 1978), was used. The best photometric model functions are listed in Table 4. For six TRAPPIST light curves (see Table 4), a normalization offset was also part of the baseline model to represent the effect of the meridian flip; that is, the 180° rotation that the German equatorial mount telescope has to undergo when the meridian is reached. This movement results in different positions of the stellar images on the detector before and after the flip, and the normalization offset allows to take into account a possible consecutive jump in the differential photometry at the time of the flip.

Concerning the RVs, a model with a trend was tested for each system. Such a trend would be indicative of the presence of an additional massive body in the system. A model with a slope was slightly favored in the case of WASP-68 with a Bayes factor ~90. We thus adopted this model for this system but the Bayes factor value is not high enough to be decisive (Jeffreys 1961) and more RVs are needed to confirm this possible trend.

The basic jump parameters in our MCMC analyses, i.e. the parameters that are randomly perturbed at each step of the MCMC, were: the planet/star area ratio $(R_{\rm p}/R_\star)^2$; the transit impact parameter in the case of a circular orbit $b' = a \cos i_{\rm p}/R_\star$ where a is the orbital semi-major axis and $i_{\rm p}$ is the orbital inclination; the transit width (from 1st to 4th contact) W; the time of mid-transit T_0; the orbital period P; the parameter $K_2 = K\sqrt{1-e^2}\,P^{1/3}$ where K is the RV orbital semi-amplitude and e is the orbital eccentricity; and the two

Table 4. Summary of follow-up photometry obtained for WASP-68, WASP-73, and WASP-88.

Target	Night	Telescope	Filter	N_p	$T_{\rm exp}$ (s)	Baseline function	σ (%)	σ_{120s} (%)	β_w	β_r	CF
WASP-68	2012 May 16–17	TRAPPIST	$I+z$	1139	8	$p(a^1+f^1+xy^1)+o$	0.28	0.10	1.03	1.22	1.26
WASP-68	2012 Jul. 06–07	TRAPPIST	$I+z$	1181	8	$p(a^2+b^1+xy^2)+o$	0.30	0.11	1.21	1.27	1.54
WASP-68	2013 Jul. 02–03	TRAPPIST	$I+z$	1357	8	$p(t^2+b^1+xy^1)+o$	0.25	0.10	0.88	1.57	1.39
WASP-68	2012 Jul. 06–07	EulerCam	I_c	412	40	$p(t^2+f^2+b^1)$	0.10	0.07	1.40	1.00	1.40
WASP-68	2013 Jul. 02–03	EulerCam	I_c	333	50	$p(a^1+f^1+xy^1)$	0.10	0.08	1.36	2.15	2.93
WASP-73	2012 Jul. 19–20	TRAPPIST	z'	476	25	$p(t^2)$	0.22	0.12	1.13	1.08	1.22
WASP-73	2012 Jul. 23–24	TRAPPIST	z'	640	25	$p(a^1+f^1)+o$	0.25	0.14	1.47	1.11	1.63
WASP-73	2012 Jul. 19–20	EulerCam	Gunn-r'	346	60	$p(t^2+f^2+xy^1)$	0.10	0.07	1.48	1.54	2.27
WASP-73	2012 Jul. 23–24	EulerCam	Gunn-r'	352	50	$p(a^1+xy^1)$	0.13	0.10	1.61	2.55	4.11
WASP-88	2012 Aug. 27–28	TRAPPIST	$I+z$	867	20	$p(a^1)+o$	0.23	0.11	1.10	1.19	1.31
WASP-88	2013 Jun. 30–Jul. 01	TRAPPIST	$I+z$	837	20	$p(t^2)+o$	0.37	0.21	1.59	1.14	1.82
WASP-88	2012 Aug. 12–13	EulerCam	Gunn-r'	95	80	$p(a^1+xy^2)$	0.08	0.08	1.25	1.00	1.25
WASP-88	2013 Jun. 25–26	EulerCam	Gunn-r'	246	70	$p(a^1+f^1)$	0.09	0.09	1.31	2.33	3.05
WASP-88	2013 Jun. 30-Jul. 01	EulerCam	Gunn-r'	317	70	$p(t^2+b^1)$	0.17	0.17	2.45	1.08	2.65

Notes. For each light curve, this table shows the date of acquisition, the used instrument and filter, the number of data points, the exposure time, the selected baseline function, the standard deviation of the best-fit residuals (unbinned and binned per intervals of 2 min), and the deduced values for β_w, β_r and $CF = \beta_w \times \beta_r$. For the baseline function, $p(\epsilon^N)$ denotes, respectively, a N-order polynomial function of time ($\epsilon = t$), airmass ($\epsilon = a$), PSF full-width at half maximum ($\epsilon = f$), background ($\epsilon = b$), and x and y positions ($\epsilon = xy$). The symbol o denotes an offset fixed at the time of the meridian flip.

parameters $\sqrt{e}\cos\omega$ and $\sqrt{e}\sin\omega$, where ω is the argument of the periastron. The reasons to use $\sqrt{e}\cos\omega$ and $\sqrt{e}\sin\omega$ as jump parameters instead of the more traditional $e\cos\omega$ and $e\sin\omega$ are detailed in Triaud et al. (2011). For all these jump parameters, we assumed a uniform prior distribution. The photometric baseline model parameters were not actual jump parameters; they were determined by a least-square minimization at each step of the MCMC.

The effect of stellar limb-darkening on our transit light curves was accounted for using a quadratic limb-darkening law, where the quadratic coefficients u_1 and u_2 were allowed to float in our MCMC analysis. However, we did not use these coefficients themselves as jump parameters but their combinations, $c_1 = 2\times u_1 + u_2$ and $c_2 = u_1 - 2\times u_2$, to minimize the correlation of the obtained uncertainties as introduced by Holman et al. (2006). To obtain a limb-darkening solution consistent with theory, we used normal prior distributions for u_1 and u_2 based on theoretical values and 1σ errors interpolated in the tables by Claret & Bloemen (2011). For the non-standard $I+z$ filter, the modes of the normal prior distributions for u_1 and u_2 were taken as the averages of the values interpolated in the tables for the standard filters I_c and z', while the errors were computed as the quadratic sums of the errors for these two filters. For the three systems, the prior distributions used for u_1 and u_2 are presented in Table 5.

For each system, a preliminary analysis was performed to determine the correction factors (CF) for our photometric errors, as described in Gillon et al. (2012). For each light curve, CF is the product of two contributions, β_w and β_r. On one side, β_w represents the under- or overestimation of the white noise of each measurement. It is computed as the ratio between the standard deviation of the residuals and the mean photometric error. On the other side, β_r allows us to take into account the correlated noise present in the light curve (i.e., the inability of our model to perfectly fit the data). It is calculated from the standard deviations of the binned and unbinned residuals for different binning intervals ranging from 5 to 120 min with the largest value being kept as β_r. The standard deviation of the best-fit residuals (unbinned and binned per intervals of 2 min) and the deduced values for β_w, β_r and $CF = \beta_w \times \beta_r$ for each light curve are presented in Table 4. For each RV time-series, a "jitter" noise was determined and added quadratically to the errors to equal their mean value to the standard deviation of the best-fit residuals. These RV jitters take into account the instrumental and astrophysical effects (such as stellar activity) that are not included in the initial error estimation. The derived jitter values were 6.6 m s^{-1} for WASP-68, 9.2 m s^{-1} for WASP-73 and 10.9 m s^{-1} for WASP-88.

Table 5. Expectations and standard deviations of the normal distributions used as prior distributions for the quadratic limb-darkening (LD) coefficients u_1 and u_2 in our MCMC analyses.

LD coefficient	WASP-68	WASP-73	WASP-88
$u_{1,I+z}$	0.256 ± 0.021	–	0.187 ± 0.016
$u_{2,I+z}$	0.283 ± 0.003	–	0.303 ± 0.005
u_{1,I_c}	0.275 ± 0.010	–	–
u_{2,I_c}	0.286 ± 0.005	–	–
$u_{1,z'}$	–	0.213 ± 0.015	–
$u_{2,z'}$	–	0.291 ± 0.005	–
$u_{1,\text{Gunn}-r'}$	–	0.349 ± 0.020	0.293 ± 0.012
$u_{2,\text{Gunn}-r'}$	–	0.301 ± 0.008	0.319 ± 0.005

Our final analyses consisted each of five Markov chains of 10^5 steps, whose convergence was checked using the statistical test of Gelman & Rubin (1992). At each step of the Markov chains, the stellar density $\rho_\star$ was derived from the Kepler's third law and the jump parameters $(R_p/R_\star)^2$, b', W, P, $\sqrt{e}\cos\omega$ and $\sqrt{e}\sin\omega$ (see e.g. Seager & Mallén-Ornelas 2003 and Winn 2010). The resulting stellar density and values for $T_{\rm eff}$ and [Fe/H] drawn from the normal distributions deduced from our spectroscopic analysis (see Sect. 3.1) were used to determine a value for the stellar mass $M_\star$ through an empirical law $M_\star(\rho_\star, T_{\rm eff}, [\text{Fe/H}])$ (Enoch et al. 2010, Gillon et al. 2011a) that is calibrated using the set of well-constrained

detached binary systems presented by Southworth (2011). For WASP-68, this set was reduced to the 116 stars with a mass between 0.7 and 1.7 $M_\odot$, while the 119 stars with a mass between 0.9 and 1.9 $M_\odot$ were used for WASP-73 and WASP-88. The goal of these selections was to benefit from our preliminary estimation of the stellar masses (see Sect. 3.1) to improve the determination of the values of the systems' parameters. To correctly propagate the error on the empirical law, the parameters of the selected subset of calibration stars were normally perturbed within their observational error bars and the coefficients of the law were redetermined at each MCMC step. The other physical parameters were then deduced from the jump parameters and stellar mass.

For each system, two analyses were performed: one assuming a circular orbit ($e = 0$) and one with a free eccentricity. For the three systems, the resulting Bayes factors (~1100 for WASP-68, ~1800 for WASP-73, and ~1800 for WASP-88) favored the circular solutions. We thus adopt the corresponding results as our nominal solutions but we present the derived parameters for both models in Table 6 (WASP-68), Table 7 (WASP-73), and Table 8 (WASP-88) for the sake of completeness. The best-fit transit models for the circular solutions are shown in Figs. 3, 5, and 7.

3.3. Stellar evolution modeling

After the completion of the MCMC analyses, we performed a stellar evolution modeling based on the CLES code (Scuflaire et al. 2008) for the three systems with the aim to assess the reliability of the deduced stellar masses and to estimate the age of the systems. We used as inputs the stellar densities deduced from the MCMC analyses, and the effective temperatures and metallicities as derived from spectroscopy (see Tables 6–8). We considered here that [Fe/H] represents the global metallicity with respect to the Sun, defined as $[\log(Z/X)_* - \log(Z/X)_\odot]$, where X and Z are the fractional mass of hydrogen and elements heavier than helium respectively. We used the most recent solar mixture of Asplund et al. (2009), which gives for the current Sun $(Z/X)_\odot = 0.0181$. The parameter of the mixing-length theory (MLT) of convection was kept fixed to the solar calibration ($\alpha_{\rm MLT} = 1.8$), and microscopic diffusion (gravitational settling) of elements was included.

The resulting stellar masses are $1.27 \pm 0.11\ M_\odot$ (WASP-68), $1.40 \pm 0.16\ M_\odot$ (WASP-73), and $1.41 \pm 0.14\ M_\odot$ (WASP-88). These 1σ uncertainties were obtained by considering the respective 1σ range for the effective temperatures, metallicities, and stellar densities but also by varying the internal stellar physics. We indeed computed, since the helium atmospheric abundance cannot be directly measured from spectroscopy, evolutionary tracks with two initial helium abundances: the solar value ($Y_\odot = 0.2485$) and a value labelled $Y_{\rm G}$ that increases with Z (as expected if the local medium follows the general trend observed for the chemical evolution of galaxies; Izotov & Thuan 2010). We also investigated the effects of the possible convective core overshooting by varying $\alpha_{\rm ov}$ between 0 and 0.3. Within the same hypotheses, the resulting stellar ages range 4.5–7.0 Gyr (WASP-68), 2.8–5.7 Gyr (WASP-73), and 1.8–4.3 Gyr (WASP-88). Three evolutionary tracks, respectively, for the central value for the stellar mass and metallicity of WASP-68, WASP-73, and WASP-88, are shown in Fig. 8. These evolutionary tracks span from the beginning (zero-age) of the main sequence to the beginning of the subgiant phase (core H-burning exhaustion). WASP-73 appears to be the most evolved star, close to or already in the subgiant phase. The stars WASP-68 and WASP-88 are less evolved, although in an advanced stage of core H-burning. The subgiant phase is also a possibility, although very unlikely.

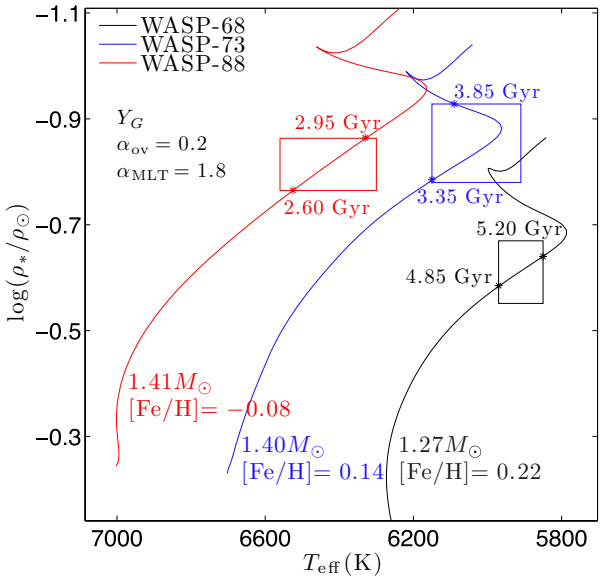

Fig. 8. Evolutionary tracks in a $T_{\rm eff} - \log(\rho_*/\rho_\odot)$ HR diagram for WASP-68 (black), WASP-73 (blue), and WASP-88 (red), for their respective central masses and metallicities. These evolutionary tracks span from the zero-age main sequence to the beginning of the subgiant phase. The ages of the stars when they cross their respective 1σ box $T_{\rm eff} - \log(\rho_*/\rho_\odot)$ are also indicated.

The masses derived for WASP-68 and WASP-88 are in excellent agreement with the MCMC results obtained through an empirical law $M_\star(\rho_\star, T_{\rm eff}, [{\rm Fe/H}])$ that is calibrated using a set of well-constrained detached eclipsing binary (EB) systems (see Sect. 3.2). The agreement is also good for WASP-73, which is close to core H-burning exhaustion or already in the subgiant phase, despite that the EB sample contains only a small fraction of significantly evolved objects. This shows that the EB empirical law used in the MCMC analyses is valid for the three stars considered here.

For even more evolved stars, the EB empirical law would reach its limit of applicability and could lead to inaccurate results. In such a case, a more reliable alternative would be to implement the stellar evolutionary models in the MCMC analysis, by assuming realistic prior probability distributions on the different stellar physics parameters (overshooting, diffusion, initial composition, etc.) and computing at each step M_* from ρ_*, $T_{\rm eff}$, and [Fe/H]. This is a long-term goal we are pursuing (e.g., Triaud et al. 2011). Obtaining an accurate stellar mass from evolution modeling primarily needs accurate spectroscopic estimates for the effective temperature but also, very importantly, for the metallicity (compare the tracks of two very close stellar masses, 1.40 $M_\odot$ and 1.41 $M_\odot$, but with quite different metallicities in Fig. 8).

4. Discussion and summary

We presented three newly discovered transiting hot Jupiters from the WASP survey, WASP-68 b, WASP-73 b, and WASP-88 b. We derived the parameters of each system from a joint analysis of the CORALIE spectroscopy and the high-precision photometry from TRAPPIST and EulerCam.

Table 6. System parameters for WASP-68.

General information		
RA (J2000)	20 20 22.98	
Dec (J2000)	–19 18 52.9	
V	10.7	
K	8.9	
Stellar parameters from spectroscopic analysis		
$T_{\rm eff}$ (K)	5910 ± 60	
$\log g_\star$ [cgs]	4.17 ± 0.11	
[Fe/H]	0.22 ± 0.08	
$\xi_{\rm t}$ (km s^{-1})	1.4 ± 0.1	
$v_{\rm mac}$ (km s^{-1})	2.6 ± 0.3	
$v \sin i_\star$ (km s^{-1})	2.3 ± 0.8	
Sp. type	G0	
Parameters from MCMC analyses		
Jump parameters	$e \geq 0$	$e = 0$ (adopted)
Planet/star area ratio $(R_{\rm p}/R_\star)^2$ [%]	0.57 ± 0.03	$0.57^{+0.03}_{-0.02}$
$b' = a \cos i_{\rm p}/R_\star$ [$R_\star$]	$0.27^{+0.16}_{-0.18}$	$0.26^{+0.15}_{-0.18}$
Transit width W [d]	$0.214^{+0.003}_{-0.002}$	$0.214^{+0.003}_{-0.002}$
T_0 [HJD$_{\rm TDB}$]	$2456064.86355^{+0.00064}_{-0.00062}$	$2456064.86356^{+0.00060}_{-0.00061}$
Orbital period P [d]	5.084299 ± 0.000015	5.084298 ± 0.000015
RV K_2 [m s^{-1} d$^{1/3}$]	168.2 ± 3.3	$168.3^{+3.2}_{-3.3}$
RV slope [m s^{-1} y^{-1}]	14 ± 2	14 ± 2
$\sqrt{e} \cos \omega$	$0.091^{+0.041}_{-0.058}$	0 (fixed)
$\sqrt{e} \sin \omega$	$-0.037^{+0.100}_{-0.091}$	0 (fixed)
$c_{1,I+z}$	0.79 ± 0.04	$0.79^{+0.05}_{-0.04}$
$c_{2,I+z}$	-0.31 ± 0.02	-0.31 ± 0.03
c_{1,I_c}	0.84 ± 0.03	0.84 ± 0.02
c_{2,I_c}	-0.29 ± 0.02	-0.29 ± 0.02
Effective temperature $T_{\rm eff}$ [K][a]	5911 ± 60	5911^{+59}_{-60}
Metallicity [Fe/H] [dex][a]	0.22 ± 0.08	0.22 ± 0.08
Deduced stellar parameters		
Mean density $\rho_\star$ [$\rho_\odot$]	$0.26^{+0.03}_{-0.05}$	$0.26^{+0.03}_{-0.05}$
Surface gravity $\log g_\star$ [cgs]	$4.09^{+0.13}_{-0.08}$	$4.09^{+0.13}_{-0.08}$
Mass $M_\star$ [$M_\odot$]	1.23 ± 0.03	1.24 ± 0.03
Radius $R_\star$ [$R_\odot$]	$1.69^{+0.13}_{-0.07}$	$1.69^{+0.11}_{-0.06}$
Luminosity $L_\star$ [$L_\odot$]	$3.1^{+0.5}_{-0.3}$	$3.2^{+0.4}_{-0.3}$
$u_{1,I+z}$	0.25 ± 0.02	$0.26^{+0.03}_{-0.02}$
$u_{2,I+z}$	0.28 ± 0.01	0.28 ± 0.01
u_{1,I_c}	0.28 ± 0.01	0.28 ± 0.01
u_{2,I_c}	0.28 ± 0.01	0.28 ± 0.01
Deduced planet parameters		
RV K [m s^{-1}]	97.9 ± 1.9	97.9 ± 1.9
Planet/star radius ratio $R_{\rm p}/R_\star$	0.075 ± 0.002	0.075 ± 0.002
$b_{\rm tr}$ [$R_\star$]	$0.27^{+0.16}_{-0.18}$	$0.26^{+0.15}_{-0.18}$
$b_{\rm oc}$ [$R_\star$]	$0.27^{+0.16}_{-0.18}$	$0.26^{+0.15}_{-0.18}$
$T_{\rm oc}$ [HJD$_{\rm TDB}$]	2456067.444 ± 0.029	2456067.406 ± 0.001
Scaled semi-major axis $a/R_\star$	$7.91^{+0.29}_{-0.50}$	$7.90^{+0.25}_{-0.46}$
Orbital semi-major axis a [AU]	$0.06204^{+0.00049}_{-0.00042}$	$0.06206^{+0.00045}_{-0.00040}$
Orbital inclination $i_{\rm p}$ [deg]	$88.1^{+1.3}_{-1.4}$	88.1 ± 1.3
Orbital eccentricity e	$0.017^{+0.012}_{-0.010}$, < 0.063 (95 %)	0 (fixed)
Argument of periastron ω [deg]	338^{+63}_{-42}	–
Mean density $\rho_{\rm p}$ [$\rho_{\rm Jup}$]	$0.50^{+0.08}_{-0.11}$	$0.50^{+0.07}_{-0.10}$
Surface gravity $\log g_{\rm p}$ [cgs]	$3.19^{+0.04}_{-0.07}$	$3.19^{+0.04}_{-0.06}$
Mass $M_{\rm p}$ [$M_{\rm Jup}$]	0.95 ± 0.03	0.95 ± 0.03
Radius $R_{\rm p}$ [$R_{\rm Jup}$]	$1.27^{+0.11}_{-0.06}$	$1.24^{+0.10}_{-0.06}$
Roche limit $a_{\rm R}$ [AU][b]	$0.01413^{+0.00130}_{-0.00075}$	$0.01415^{+0.00120}_{-0.00065}$
$a/a_{\rm R}$	$4.39^{+0.23}_{-0.35}$	$4.38^{+0.19}_{-0.32}$
Equilibrium temperature $T_{\rm eq}$ [K][c]	1488^{+49}_{-32}	1490^{+44}_{-29}
Irradiation [erg s^{-1}cm^{-2}]	$1.1^{+0.3}_{-0.2}\ 10^9$	$1.1^{+0.3}_{-0.2}\ 10^9$

Notes. The values given for the parameters derived from our MCMC analyses are medians and 1σ limits of the marginalized posterior probability distributions. [(a)] Using as priors the values derived from the spectroscopic analysis. [(b)] Using $a_{\rm R} = 2.46\ R_{\rm p}(M_\star/M_{\rm p})^{1/3}$ (Chandrasekhar 1987). [(c)] Assuming a null Bond albedo and an efficient heat distribution between both hemispheres.

Table 7. System parameters for WASP-73.

General information		
RA (J2000)	21 19 47.91	
Dec (J2000)	–58 08 56.0	
V	10.5	
K	9.0	
Stellar parameters from spectroscopic analysis		
$T_{\rm eff}$ (K)	6030 ± 120	
log $g_\star$	3.92 ± 0.08	
[Fe/H]	0.14 ± 0.14	
$\xi_{\rm t}$ (km s^{-1})	1.1 ± 0.2	
$v_{\rm mac}$ (km s^{-1})	3.3 ± 0.3	
$v \sin i_\star$ (km s^{-1})	6.1 ± 0.6	
Sp. type	F9	
Parameters from MCMC analyses		
Jump parameters	$e \geq 0$	$e = 0$ (adopted)
Planet/star area ratio $(R_{\rm p}/R_\star)^2$ [%]	0.33 ± 0.03	0.33 ± 0.03
$b' = a \cos i_{\rm p}/R_\star$ [$R_\star$]	$0.26^{+0.20}_{-0.17}$	$0.26^{+0.20}_{-0.18}$
Transit width W [d]	0.233 ± 0.003	0.233 ± 0.003
T_0 [HJD$_{\rm TDB}$]	2456128.7063 ± 0.0011	2456128.7063 ± 0.0011
Orbital period P [d]	4.08721 ± 0.00022	4.08722 ± 0.00022
RV K_2 [m s^{-1} d$^{1/3}$]	313.5 ± 6.9	313.9 ± 6.6
$\sqrt{e} \cos \omega$	$-0.021^{+0.065}_{-0.061}$	0 (fixed)
$\sqrt{e} \sin \omega$	$0.039^{+0.100}_{-0.110}$	0 (fixed)
$c_{1,z'}$	0.71 ± 0.03	$0.71^{+0.04}_{-0.03}$
$c_{2,z'}$	–0.37 ± 0.02	–0.37 ± 0.02
$c_{1,{\rm Gunn}-r'}$	$1.01^{+0.04}_{-0.05}$	$1.01^{+0.04}_{-0.05}$
$c_{2,{\rm Gunn}-r'}$	–0.25 ± 0.03	–0.25 ± 0.03
Effective temperature $T_{\rm eff}$ [K]^a	6030 ± 120	6036 ± 120
Metallicity [Fe/H] [dex]^a	0.14 ± 0.14	0.14 ± 0.14
Deduced stellar parameters		
Mean density $\rho_\star$ [$\rho_\odot$]	$0.15^{+0.02}_{-0.03}$	$0.15^{+0.02}_{-0.04}$
Surface gravity log $g_\star$ [cgs]	$3.92^{+0.04}_{-0.06}$	$3.93^{+0.04}_{-0.06}$
Mass $M_\star$ [$M_\odot$]	$1.34^{+0.05}_{-0.04}$	$1.34^{+0.05}_{-0.04}$
Radius $R_\star$ [$R_\odot$]	$2.09^{+0.18}_{-0.09}$	$2.07^{+0.19}_{-0.08}$
Luminosity $L_\star$ [$L_\odot$]	$5.2^{+1.0}_{-0.7}$	$5.2^{+1.0}_{-0.6}$
$u_{1,z'}$	0.21 ± 0.02	0.21 ± 0.02
$u_{2,z'}$	0.29 ± 0.01	0.29 ± 0.01
$u_{1,{\rm Gunn}-r'}$	0.35 ± 0.03	0.35 ± 0.03
$u_{2,{\rm Gunn}-r'}$	0.30 ± 0.01	0.30 ± 0.01
Deduced planet parameters		
RV K [m s^{-1}]	196.1 ± 4.3	196.3 ± 4.1
Planet/star radius ratio $R_{\rm p}/R_\star$	0.057 ± 0.003	0.057 ± 0.003
$b_{\rm tr}$ [$R_\star$]	$0.25^{+0.20}_{-0.17}$	$0.26^{+0.20}_{-0.18}$
$b_{\rm oc}$ [$R_\star$]	$0.26^{+0.20}_{-0.17}$	$0.26^{+0.20}_{-0.18}$
$T_{\rm oc}$ [HJD$_{\rm TDB}$]	$2456130.746^{+0.013}_{-0.021}$	2456130.750 ± 0.002
Scaled semi-major axis $a/R_\star$	$5.68^{+0.21}_{-0.42}$	$5.73^{+0.18}_{-0.45}$
Orbital semi-major axis a [AU]	$0.05514^{+0.00061}_{-0.00054}$	$0.05512^{+0.00060}_{-0.00053}$
Orbital inclination $i_{\rm p}$ [deg]	$87.4^{+1.8}_{-2.4}$	$87.4^{+1.8}_{-2.4}$
Orbital eccentricity e	$0.011^{+0.015}_{-0.008}$, < 0.074 (95 %)	0 (fixed)
Argument of periastron ω [deg]	108^{+110}_{-68}	–
Mean density $\rho_{\rm p}$ [$\rho_{\rm Jup}$]	$1.19^{+0.25}_{-0.29}$	$1.20^{+0.26}_{-0.30}$
Surface gravity log $g_{\rm p}$ [cgs]	$3.54^{+0.06}_{-0.08}$	$3.54^{+0.06}_{-0.08}$
Mass $M_{\rm p}$ [$M_{\rm Jup}$]	1.88 ± 0.06	$1.88^{+0.07}_{-0.06}$
Radius $R_{\rm p}$ [$R_{\rm Jup}$]	$1.16^{+0.12}_{-0.08}$	$1.16^{+0.12}_{-0.08}$
Roche limit $a_{\rm R}$ [AU]^b	$0.01090^{+0.00120}_{-0.00072}$	$0.01089^{+0.00120}_{-0.00072}$
$a/a_{\rm R}$	$5.05^{+0.34}_{-0.45}$	$5.07^{+0.34}_{-0.46}$
Equilibrium temperature $T_{\rm eq}$ [K]^c	1795^{+73}_{-52}	1790^{+75}_{-51}
Irradiation [erg s^{-1}cm^{-2}]	$2.4^{+0.7}_{-0.4}\ 10^9$	$2.3^{+0.8}_{-0.4}\ 10^9$

Notes. The values given for the parameters derived from our MCMC analyses are medians and 1σ limits of the marginalized posterior probability distributions. $^{(a)}$ Using as priors the values derived from the spectroscopic analysis. $^{(b)}$ Using $a_{\rm R} = 2.46\ R_{\rm p}(M_\star/M_{\rm p})^{1/3}$ (Chandrasekhar 1987). $^{(c)}$ Assuming a null Bond albedo and an efficient heat distribution between both hemispheres.

Table 8. System parameters for WASP-88.

General information		
RA (J2000)	20 38 02.70	
Dec (J2000)	–48 27 43.2	
V	11.4	
K	10.3	
Stellar parameters from spectroscopic analysis		
$T_{\rm eff}$ (K)	6430 ± 130	
log $g_\star$	4.03 ± 0.09	
[Fe/H]	–0.08 ± 0.12	
$\xi_{\rm t}$ (km s^{-1})	1.4 ± 0.1	
$v_{\rm mac}$ (km s^{-1})	4.7 ± 0.3	
$v \sin i_\star$ (km s^{-1})	8.4 ± 0.8	
Sp. type	F6	
Parameters from MCMC analyses		
Jump parameters	$e \geq 0$	$e = 0$ (adopted)
Planet/star area ratio $(R_{\rm p}/R_\star)^2$ [%]	$0.71^{+0.04}_{-0.03}$	0.70 ± 0.03
$b' = a \cos i_{\rm p}/R_\star$ [$R_\star$]	$0.24^{+0.15}_{-0.16}$	0.23 ± 0.15
Transit width W [d]	$0.252^{+0.003}_{-0.002}$	$0.252^{+0.003}_{-0.002}$
T_0 [HJD$_{\rm TDB}$]	$2456474.73145^{+0.00084}_{-0.00089}$	$2456474.73154^{+0.00085}_{-0.00086}$
Orbital period P [d]	4.954000 ± 0.000019	4.954000 ± 0.000019
RV K_2 [m s^{-1} d$^{1/3}$]	90.3 ± 11.0	89.4 ± 11.0
$\sqrt{e} \cos \omega$	$-0.147^{+0.190}_{-0.140}$	0 (fixed)
$\sqrt{e} \sin \omega$	$-0.010^{+0.260}_{-0.250}$	0 (fixed)
$c_{1,I+z}$	0.67 ± 0.04	0.67 ± 0.04
$c_{2,I+z}$	–0.42 ± 0.02	–0.42 ± 0.02
$c_{1,{\rm Gunn}-r'}$	0.90 ± 0.03	0.90 ± 0.03
$c_{2,{\rm Gunn}-r'}$	–0.35 ± 0.02	–0.35 ± 0.02
Effective temperature $T_{\rm eff}$ [K][a]	6431 ± 130	6431 ± 130
Metallicity [Fe/H] [dex][a]	–0.08 ± 0.12	–0.08 ± 0.12
Deduced stellar parameters		
Mean density $\rho_\star$ [$\rho_\odot$]	$0.16^{+0.05}_{-0.04}$	$0.16^{+0.02}_{-0.03}$
Surface gravity log $g_\star$ [cgs]	$3.95^{+0.07}_{-0.09}$	$3.96^{+0.02}_{-0.05}$
Mass $M_\star$ [$M_\odot$]	1.45 ± 0.06	1.45 ± 0.05
Radius $R_\star$ [$R_\odot$]	$2.10^{+0.24}_{-0.18}$	$2.08^{+0.12}_{-0.06}$
Luminosity $L_\star$ [$L_\odot$]	$6.8^{+1.7}_{-1.3}$	$6.8^{+1.0}_{-0.8}$
$u_{1,I+z}$	0.18 ± 0.02	0.18 ± 0.02
$u_{2,I+z}$	0.30 ± 0.01	0.30 ± 0.01
$u_{1,{\rm Gunn}-r'}$	0.29 ± 0.02	0.29 ± 0.02
$u_{2,{\rm Gunn}-r'}$	0.32 ± 0.01	0.32 ± 0.01
Deduced planet parameters		
RV K [m s^{-1}]	$53.4^{+6.8}_{-6.6}$	52.4 ± 6.6
Planet/star radius ratio $R_{\rm p}/R_\star$	0.084 ± 0.002	0.084 ± 0.002
$b_{\rm tr}$ [$R_\star$]	$0.24^{+0.15}_{-0.16}$	0.23 ± 0.15
$b_{\rm oc}$ [$R_\star$]	$0.24^{+0.16}_{-0.15}$	0.23 ± 0.15
$T_{\rm oc}$ [HJD$_{\rm TDB}$]	$2456472.135^{+0.146}_{-0.220}$	2456477.20854 ± 0.00086
Scaled semi-major axis $a/R_\star$	$6.58^{+0.56}_{-0.60}$	$6.64^{+0.17}_{-0.34}$
Orbital semi-major axis a [AU]	$0.06432^{+0.00088}_{-0.00083}$	$0.06431^{+0.00065}_{-0.00062}$
Orbital inclination $i_{\rm p}$ [deg]	$87.9^{+1.4}_{-1.6}$	$88.0^{+1.4}_{-1.5}$
Orbital eccentricity e	$0.082^{+0.084}_{-0.057}$, < 0.482 (95 %)	0 (fixed)
Argument of periastron ω [deg]	191^{+75}_{-79}	–
Mean density $\rho_{\rm p}$ [$\rho_{\rm Jup}$]	0.11 ± 0.04	0.11 ± 0.03
Surface gravity log $g_{\rm p}$ [cgs]	$2.67^{+0.10}_{-0.11}$	$2.67^{+0.07}_{-0.08}$
Mass $M_{\rm p}$ [$M_{\rm Jup}$]	0.57 ± 0.08	0.56 ± 0.08
Radius $R_{\rm p}$ [$R_{\rm Jup}$]	$1.72^{+0.21}_{-0.16}$	$1.70^{+0.13}_{-0.07}$
Roche limit $a_{\rm R}$ [AU][b]	$0.02470^{+0.00330}_{-0.00250}$	$0.02464^{+0.00210}_{-0.00150}$
$a/a_{\rm R}$	$2.60^{+0.28}_{-0.29}$	$2.61^{+0.16}_{-0.19}$
Equilibrium temperature $T_{\rm eq}$ [K][c]	1775^{+93}_{-83}	1772^{+54}_{-45}
Irradiation [erg s^{-1}cm^{-2}]	$2.3^{+0.9}_{-1.1}\ 10^9$	$2.2^{+0.5}_{-0.3}\ 10^9$

Notes. The values given for the parameters derived from our MCMC analyses are medians and 1σ limits of the marginalized posterior probability distributions. [(a)] Using as priors the values derived from the spectroscopic analysis. [(b)] Using $a_{\rm R} = 2.46\ R_{\rm p}(M_\star/M_{\rm p})^{1/3}$ (Chandrasekhar 1987). [(c)] Assuming a null Bond albedo and an efficient heat distribution between both hemispheres.

All three host stars appear to be significantly evolved (especially WASP-73, see Sect. 3.3) and thus have relatively large radii (1.7–2.2 $R_\odot$). At the time of writing, only about 20 transiting hot Jupiters have been found to orbit such large stars[4]. This small number of detections might be due to the fact that large stellar radii translate into relatively shallow transits for the potential orbiting planets. These transits are therefore more difficult to detect by ground-based transit surveys. Alternatively, this might also be indicative of the tidal destruction of hot Jupiters. Due to their relatively large masses and small semi-major axes, hot Jupiters are expected to undergo tidal transfers of angular momentum with their host stars (e.g. Barker & Ogilvie 2009), which should lead to a slow spiral-in of the planets in most cases, until they are finally disrupted at their Roche limits (Gu et al. 2003). Although the timescale for orbital decay is quite uncertain and different for each system, it would thus not be surprising to find fewer close-in giant planets around larger and older stars, as there is a higher probability that these planets, if they once existed, have already been tidally disrupted. However, this correlation between the occurrence of hot Jupiters and the systems' ages has not been demonstrated yet.

It is also now common knowledge that tidal interactions tend to realign hot Jupiters' orbits with their host stars' equatorial planes (see Barker & Ogilvie 2009). Triaud (2011) demonstrated, using spin/orbit measurements for 22 hot Jupiters around stars with masses $\geq$1.2 $M_\odot$, the existence of a correlation between these hot Jupiters' orbital obliquities and their ages and estimated the typical timescale for a non-coplanar hot Jupiter's orbit to tidally realign to be about 2.5 Gyr. Considering the estimated ages of our three systems, we can therefore expect their orbits to have realigned. However, it would be interesting to perform Rossiter-McLaughlin effect observations to confirm this tendency.

Due to the large radii of their host stars, our three planets are exposed to a relatively high irradiation (incident flux $>10^9$ erg s^{-1} cm^{-2}). Several works showed that hot Jupiters' radii correlate well with their irradiating flux (see e.g. Demory & Seager 2011; Enoch et al. 2012; or Weiss et al. 2013). Figure 9 shows the positions of our three planets in an irradiation-radius diagram for the known transiting planets with 0.5 $M_{\rm Jup}$ < $M_{\rm p}$ < 2 $M_{\rm Jup}$ and P < 12 d. WASP-68 b lies in a well-populated region of the diagram. Its physical dimensions can be considered as rather standard. Indeed, its measured radius of $1.24^{+0.10}_{-0.06}$ $R_{\rm Jup}$ is in perfect agreement with the value of 1.24 ± 0.03 $R_{\rm Jup}$ predicted by the equation derived by Weiss et al. (2013) from a sample of 103 transiting planets with a mass between 150 $M_\oplus$ and 13 $M_{\rm Jup}$ and that relates planets' sizes to their masses and irradiations. For WASP-73 b, the Weiss et al.'s law gives a radius of $1.29^{+0.04}_{-0.02}$ $R_{\rm Jup}$, which is slightly larger than our measured radius of $1.16^{+0.12}_{-0.08}$ $R_{\rm Jup}$. This might suggest a possible small enrichment of the planet in heavy elements. Its density of $1.20^{+0.26}_{-0.30}$ $\rho_{\rm Jup}$ is indeed surprisingly high, given the important irradiation the planet is exposed to ($\sim 2.3 \times 10^9$ erg s^{-1} cm^{-2}). However, the errors on its physical parameters are still too high to draw any strong inference on its internal structure.

Unlike the first two planets, WASP-88 b appears to be a clear outlier, its measured radius of $1.70^{+0.13}_{-0.07}$ $R_{\rm Jup}$ being significantly higher than the predicted value of 1.35 ± 0.02 $R_{\rm Jup}$. With a density of 0.11 ± 0.03 $\rho_{\rm Jup}$, WASP-88 b is actually the second least dense transiting planet known to date, tied with Kepler-12 b (Fortney et al. 2011), which also has a density around 0.11 $\rho_{\rm Jup}$. Only WASP-17 b has a lower density

[4] http://exoplanet.eu/

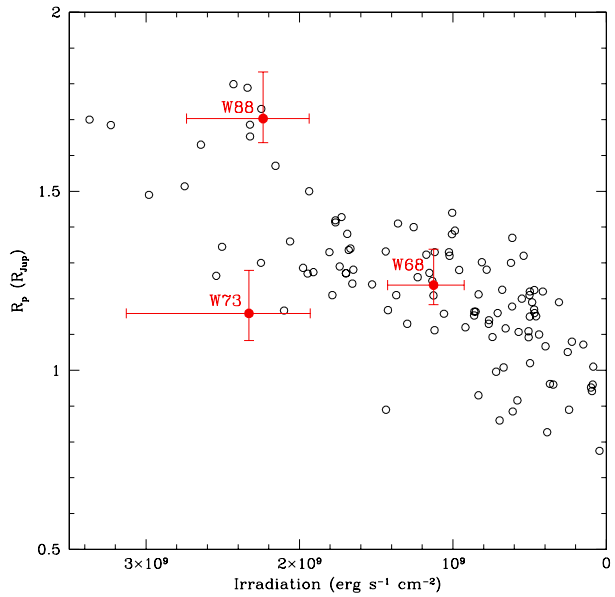

Fig. 9. Irradiation–radius diagram for the known transiting hot Jupiters with 0.5 $M_{\rm Jup}$ < $M_{\rm p}$ < 2 $M_{\rm Jup}$ and P < 12 d (data from the NASA Exoplanet Archive). The planets WASP-68 b, WASP-73 b and WASP-88 b are shown in red.

($\rho_{\rm p} = 0.06\,\rho_{\rm Jup}$, Anderson et al. 2011, Southworth et al. 2012). WASP-88 b thus joins the handful of planets with super-inflated radii. Its large radius might be explained, at least partially, by the low metallicity ([Fe/H] = -0.08 ± 0.12) of its star. With a mass of 0.56 $M_{\rm Jup}$, WASP-88 b is actually more Saturn-like than Jupiter-like and Enoch et al. (2011), basing on 18 transiting exoplanets with masses below 0.6 $M_{\rm p}$, found that there is a strong negative correlation between the star metallicity [Fe/H] and $R_{\rm p}$ for these planets. Keeping in mind that the chemical composition of a planet should be related to the one of its host star as they formed from the same cloud, the observation that the correlation between [Fe/H] and $R_{\rm p}$ is negligible for more massive planets agrees well with the theoretical planet models of Fortney et al. (2007) and Baraffe et al. (2008), which both suggest that the radius of a planet is more sensitive to its composition for low mass planets than it is for more massive ones. The relation (3) of Enoch et al. (2011) leads to a predicted radius of 1.51 ± 0.06 $R_{\rm Jup}$ for WASP-88 b, which is better than the value of Weiss et al. (2013) but still lower than our measured value. As WASP-88 b is the youngest of our three planets (see Sect. 3.3), tidal circularization and dissipation might have occurred recently enough to contribute to the observed inflated radius (see e.g. Leconte et al. 2010). Other physical mechanisms might also be at play, such as the deposition of kinetic energy into the planet from strong winds driven by the large day/night temperature contrast (Showman & Guillot 2002), reduced heat transport efficiency by layered convection inside the planet (Chabrier & Baraffe 2007), or Ohmic heating from currents induced through winds in the planetary atmosphere (Batygin & Stevenson 2010).

Acknowledgements. WASP-South is hosted by the South African Astronomical Observatory and we are grateful for their ongoing support and assistance. Funding for WASP comes from consortium universities and from UK's Science and Technology Facilities Council. TRAPPIST is a project funded by the Belgian Fund for Scientific Research (Fonds National de la Recherche Scientifique, F.R.S.-FNRS) under grant FRFC 2.5.594.09.F, with the participation of the Swiss National Science Fundation (SNF). L. Delrez acknowledges the support of the F.R.I.A. fund of the FNRS. M. Gillon and E. Jehin are FNRS Research Associates. A. H. M. J. Triaud received funding from a fellowship provided by the Swiss National Science Foundation under grant number PBGEP2-14559. We thank the anonymous referee for his valuable suggestions.

References

Anderson, D. R., Smith, A. M. S., Lanotte, A. A., et al. 2011, MNRAS, 416, 2108
Asplund, M., Grevesse, N., Sauval, A. J., & Scott, P. 2009, ARA&A, 47, 481
Baraffe, I., Chabrier, G., & Barman, T. 2008, A&A, 482, 315
Barker, A. J., & Ogilvie, G. I. 2009, MNRAS, 395, 2268
Batygin, K., & Stevenson, D. J. 2010, ApJ, 714, L238
Broeg, C., Fortier, A., Ehrenreich, D., et al. 2013, EPJ Web Conf., 47, 3005
Bruntt, H., Bedding, T. R., Quirion, P.-O., et al. 2010, MNRAS, 405, 1907
Chabrier, G., & Baraffe, I. 2007, ApJ, 661, L81
Chandrasekhar, S. 1987, Ellipsoidal figures of equilibrium
Charbonneau, D., Brown, T. M., Latham, D. W., & Mayor, M. 2000, ApJ, 529, L45
Claret, A., & Bloemen, S. 2011, A&A, 529, A75
Collier Cameron, A., Pollacco, D., Street, R. A., et al. 2006, MNRAS, 373, 799
Collier Cameron, A., Wilson, D. M., West, R. G., et al. 2007, MNRAS, 380, 1230
Demory, B.-O., & Seager, S. 2011, ApJS, 197, 12
Doyle, A. P., Smalley, B., Maxted, P. F. L., et al. 2013, MNRAS, 428, 3164
Enoch, B., Collier Cameron, A., Parley, N. R., & Hebb, L. 2010, A&A, 516, A33
Enoch, B., Cameron, A. C., Anderson, D. R., et al. 2011, MNRAS, 410, 1631
Enoch, B., Collier Cameron, A., & Horne, K. 2012, A&A, 540, A99
Fortney, J. J., Marley, M. S., & Barnes, J. W. 2007, ApJ, 659, 1661
Fortney, J. J., Demory, B.-O., Désert, J.-M., et al. 2011, ApJS, 197, 9
Gardner, J. P., Mather, J. C., Clampin, M., et al. 2006, Space Sci. Rev., 123, 485
Gelman, A., & Rubin, D. 1992, Stat. Sci., 7, 457
Gillon, M., Doyle, A. P., Lendl, M., et al. 2011a, A&A, 533, A88
Gillon, M., Jehin, E., Magain, P., et al. 2011b, EPJ Web Conf., 11, 6002
Gillon, M., Triaud, A. H. M. J., Fortney, J. J., et al. 2012, A&A, 542, A4
Gray, D. F. 2008, The Observation and Analysis of Stellar Photospheres
Gu, P.-G., Lin, D. N. C., & Bodenheimer, P. H. 2003, ApJ, 588, 509
Hellier, C., Anderson, D. R., Collier Cameron, A., et al. 2013 [arXiv:1310.5630]
Holman, M. J., Winn, J. N., Latham, D. W., et al. 2006, ApJ, 652, 1715
Izotov, Y. I., & Thuan, T. X. 2010, ApJ, 710, L67
Jeffreys, H. 1961, The Theory of Probability (New-York: Oxford University Press)
Jehin, E., Gillon, M., Queloz, D., et al. 2011, The Messenger, 145, 2
Leconte, J., Chabrier, G., Baraffe, I., & Levrard, B. 2010, A&A, 516, A64
Lendl, M., Anderson, D. R., Collier-Cameron, A., et al. 2012, A&A, 544, A72
Magain, P. 1984, A&A, 134, 189
Mandel, K., & Agol, E. 2002, ApJ, 580, L171
Maxted, P. F. L., Anderson, D. R., Collier Cameron, A., et al. 2011, PASP, 123, 547
Mayor, M., & Queloz, D. 1995, Nature, 378, 355
Murray, C. D., & Correia, A. C. M. 2010, in Exoplanets, ed. S. Seager, 15
Pepe, F., Mayor, M., Galland, F., et al. 2002, A&A, 388, 632
Pollacco, D. L., Skillen, I., Collier Cameron, A., et al. 2006, PASP, 118, 1407
Queloz, D., Henry, G. W., Sivan, J. P., et al. 2001, A&A, 379, 279
Santos, N. C., Mayor, M., Naef, D., et al. 2002, A&A, 392, 215
Schwarz, G. E. 1978, Ann. Statist., 6, 461
Scuflaire, R., Théado, S., Montalbán, J., et al. 2008, Ap&SS, 316, 83
Seager, S., & Deming, D. 2010, ARA&A, 48, 631
Seager, S., & Mallén-Ornelas, G. 2003, ApJ, 585, 1038
Showman, A. P., & Guillot, T. 2002, A&A, 385, 166
Southworth, J. 2011, MNRAS, 417, 2166
Southworth, J., Hinse, T. C., Dominik, M., et al. 2012, MNRAS, 426, 1338
Stetson, P. B. 1987, PASP, 99, 191
Torres, G., Andersen, J., & Giménez, A. 2010, A&ARv, 18, 67
Triaud, A. H. M. J. 2011, A&A, 534, L6
Triaud, A. H. M. J., Queloz, D., Hellier, C., et al. 2011, A&A, 531, A24
Weiss, L. M., Marcy, G. W., Rowe, J. F., et al. 2013, ApJ, 768, 14
Winn, J. N. 2010, in Exoplanets, ed. S. Seager, 55

Page 13 is available in the electronic edition of the journal at http://www.aanda.org

Table 1. CORALIE radial-velocity measurements for WASP-68 (BS = bisector spans).

Target	HJD_{TDB} – 2 450 000	RV (km s^{-1})	σ_{RV} (km s^{-1})	BS (km s^{-1})
WASP-68	5706.775395	28.35403	0.00736	0.02521
WASP-68	5707.797750	28.39089	0.00525	–0.01458
WASP-68	5713.793654	28.31392	0.00599	0.00789
WASP-68	5715.766225	28.21345	0.00502	0.00389
WASP-68	5722.816076	28.38649	0.00448	–0.01517
WASP-68	5765.753050	28.22263	0.00584	0.02314
WASP-68	5767.749560	28.33343	0.00634	0.00869
WASP-68	5768.728542	28.38024	0.00531	–0.00094
WASP-68	5769.731770	28.32243	0.00462	0.00260
WASP-68	5770.769094	28.21813	0.00556	0.01505
WASP-68	5772.795194	28.33309	0.01445	–0.00200
WASP-68	5777.773957	28.32040	0.00529	0.01429
WASP-68	5794.600961	28.38663	0.00517	0.01427
WASP-68	5796.549753	28.20522	0.00560	0.00768
WASP-68	5806.645082	28.20412	0.00591	0.03023
WASP-68	5807.705562	28.25392	0.00629	0.00704
WASP-68	5823.546584	28.32236	0.00642	–0.00127
WASP-68	5824.573366	28.40896	0.00536	0.02367
WASP-68	5826.655256	28.23628	0.00743	0.01630
WASP-68	5852.532499	28.19375	0.00628	–0.01225
WASP-68	5856.597408	28.28718	0.00557	–0.00265
WASP-68	5858.529438	28.25969	0.00773	–0.01544
WASP-68	5864.564865	28.35191	0.00526	–0.00650
WASP-68	5883.548579	28.23114	0.00637	0.02525
WASP-68	6021.899684	28.32750	0.00537	–0.01018
WASP-68	6022.905102	28.41331	0.00562	–0.01400
WASP-68	6048.914901	28.37000	0.00565	–0.00286
WASP-68	6067.850937	28.35299	0.00479	–0.00075
WASP-68	6076.878089	28.21947	0.00857	–0.02511
WASP-68	6103.663851	28.37654	0.00503	0.00509
WASP-68	6130.635583	28.36594	0.00871	0.04089
WASP-68	6135.775843	28.35722	0.00625	–0.01097
WASP-68	6150.631492	28.38702	0.00600	0.00044
WASP-68	6183.679884	28.22057	0.00490	0.01819
WASP-68	6184.656200	28.34522	0.00505	–0.00802
WASP-68	6204.554305	28.29089	0.00749	–0.00338
WASP-68	6216.592455	28.40205	0.00616	0.00275
WASP-68	6431.931490	28.23109	0.00612	–0.00857
WASP-68	6451.773166	28.26579	0.00488	–0.02323
WASP-68	6475.858923	28.41736	0.00631	0.02107
WASP-68	6485.724714	28.43317	0.00545	–0.00978
WASP-68	6507.676974	28.27546	0.00620	0.01077
WASP-68	6530.605288	28.38629	0.00738	0.02674

Table 2. CORALIE radial-velocity measurements for WASP-73 (BS = bisector spans).

Target	HJD_{TDB}–2 450 000	RV (km s^{-1})	σ_{RV} (km s^{-1})	BS (km s^{-1})
WASP-73	5835.606190	10.44179	0.00903	0.03075
WASP-73	5837.502076	10.82294	0.00706	0.03546
WASP-73	5851.645089	10.41902	0.00743	–0.02858
WASP-73	5856.643946	10.54277	0.00765	0.05603
WASP-73	5858.553071	10.75127	0.00964	0.02465
WASP-73	5859.533285	10.45047	0.00741	0.06098
WASP-73	5864.601220	10.48392	0.00712	0.03086
WASP-73	5865.620159	10.76933	0.00854	0.05479
WASP-73	5880.549374	10.44138	0.00782	–0.00327
WASP-73	5892.578470	10.45665	0.01222	0.04721
WASP-73	5893.565583	10.60197	0.00777	–0.00459
WASP-73	5894.530903	10.80197	0.00737	0.04810
WASP-73	6130.697716	10.60558	0.01486	0.01835
WASP-73	6137.897482	10.43505	0.01011	0.00469
WASP-73	6149.772409	10.48072	0.00869	0.03588
WASP-73	6158.765097	10.48112	0.00869	0.06660
WASP-73	6216.615675	10.64684	0.00874	0.04270
WASP-73	6488.833899	10.50459	0.00852	–0.02173
WASP-73	6546.740705	10.41467	0.00873	0.05445
WASP-73	6547.703915	10.64815	0.00711	0.02528

Table 3. CORALIE radial-velocity measurements for WASP-88 (BS = bisector spans).

Target	HJD_{TDB}–2 450 000	RV (km s^{-1})	σ_{RV} (km s^{-1})	BS (km s^{-1})
WASP-88	5834.557656	–6.75688	0.01797	0.11267
WASP-88	5856.620397	–6.82192	0.02419	0.13488
WASP-88	6119.775893	–6.80810	0.01712	0.00269
WASP-88	6121.751740	–6.72092	0.01950	0.11340
WASP-88	6123.632372	–6.81181	0.01996	0.02430
WASP-88	6124.600910	–6.86256	0.01764	0.03914
WASP-88	6125.676195	–6.77344	0.01717	–0.03997
WASP-88	6133.736344	–6.80539	0.02057	0.00683
WASP-88	6134.833084	–6.79385	0.03092	0.03759
WASP-88	6135.804118	–6.76124	0.02268	–0.02308
WASP-88	6136.820069	–6.74445	0.02080	–0.02308
WASP-88	6137.869386	–6.77739	0.02396	0.11208
WASP-88	6149.574773	–6.80985	0.02288	0.03215
WASP-88	6150.543194	–6.73250	0.02512	0.05769
WASP-88	6154.586060	–6.76785	0.02499	0.06009
WASP-88	6172.627045	–6.84122	0.01786	–0.00501
WASP-88	6173.706647	–6.87322	0.03670	0.02791
WASP-88	6475.892228	–6.83574	0.02268	0.02641
WASP-88	6480.804868	–6.82613	0.02960	0.05213
WASP-88	6487.935947	–6.70113	0.02136	0.08684
WASP-88	6558.499522	–6.76226	0.02015	0.05448
WASP-88	6563.582029	–6.71375	0.03003	–0.02524
WASP-88	6567.558431	–6.70463	0.01769	0.03362